


## Information extraction in photon-counting experiments

Timon Schapeler<sup>✉\*</sup> and Tim J. Bartley<sup>✉</sup>

*Mesoscopic Quantum Optics, Paderborn University, Warburger Straße 100, 33098 Paderborn, Germany*

 (Received 17 February 2022; accepted 21 June 2022; published 5 July 2022)

We demonstrate a comparison of different multiplexing architectures based on quantum detector tomography. Using the purity of their measurement outcomes, we gain insight into the photon-number-resolving ability of the devices. Further, we calculate the information each measurement outcome can extract from a Hilbert space with given dimension. Our work confirms that more multiplexing outcomes enable higher photon-number-resolving ability; however, the splitting between those outcomes must be optimized as well.

DOI: [10.1103/PhysRevA.106.013701](https://doi.org/10.1103/PhysRevA.106.013701)

### I. INTRODUCTION

The ability to count photons is crucial for quantum optical experiments and technologies, such as quantum metrology [1], quantum information [2], and single-photon imaging [3]. Many types of single-photon detectors have been demonstrated, all with certain advantages and disadvantages. The quality of these detectors can be quantified by many figures of merit, such as efficiency, dark counts, or timing resolution [4]. However, the ability of a detector to resolve the number of photons is a crucial quantifier in photon-counting experiments.

Resolving the photon number can be fully achieved using, for example, superconducting transition-edge sensors (TESs) [5]. For monochromatic light, a TES has full photon-number-resolving ability, which means that a specific photon number maps to a specific output signal. Some information about photon number can be obtained using click detectors such as superconducting nanowire single-photon detectors (SNSPDs) or single-photon avalanche diodes in combination with multiplexing schemes. However, multiplexing can only achieve quasi-photon-number resolution, as some information is lost due to the nonzero probability of multiple photons causing the same outcome [6].

Many different multiplexing architectures have been shown. Some of these schemes rely on equally splitting the incoming light onto the detectors, such as the conventional spatial [7] and temporal [8,9] multiplexing trees or detector arrays [10]. Others make use of logarithmic multiplexing such as the time-loop detectors [11] or integrated in-line detector arrays [12].

Multiplexed detectors can be parameterized by figures of merit such as efficiency, dark counts, and crosstalk [4,13]. Although these quantities provide intuition of the quality of the detectors, they do not quantify how these figures of merit combine to determine the utility of the devices for certain

tasks. The photon-number-resolving ability of the device is one important example which is not directly described by these figures of merit.

To overcome this limitation, van Enk introduced the concept of measurement outcome purity [14], which can be directly linked to the ability of a detector architecture to resolve photon number. A related question arises: How much information can be extracted by a measurement outcome? In this paper we experimentally investigate measurement outcome purity and information extraction for a variety of different detectors to quantify and compare their photon-number-resolving ability.

### II. MEASUREMENT OUTCOME PURITY

The specific detector architectures we consider are shown in Figs. 1(a)–1(d). In order to compare the different devices in a common framework, we use quantum detector tomography [16], which yields a quantum mechanical description of a detector under test (DUT) in terms of its so-called positive-operator-valued measures (POVMs). The set of POVMs  $\{\pi_n\}$  fully describes the detector with different outcomes  $n$ . The operators are non-negative  $\pi_n > 0$  with  $\sum_n \pi_n = 1$ .

An important property of a general detection scheme is that repeated measurements do not necessarily yield the same outcome, i.e., a measurement may not necessarily project onto pure states. van Enk [14] showed that it is thus possible to define a measurement outcome purity of the POVM corresponding to outcome  $n$ , which is analogous to the purity of a quantum state, as

$$\text{Pur}(\pi_n) = \frac{\text{Tr}[(\pi_n)^2]}{[\text{Tr}(\pi_n)]^2}. \quad (1)$$

The purity is upper bounded by unity, as a perfect measurement would be a one-to-one mapping of one input state to one outcome. The lower bound is given by the Hilbert space dimension  $M$  as  $\frac{1}{M} \leq \text{Pur}(\pi_n) \leq 1$ . A nonpure POVM means that multiple orthogonal input states contribute to the same outcome with significant probabilities [14]. It is possible to estimate the number of orthogonal input states which contribute to outcome  $n$  by the inverse of the purity  $\text{Pur}(\pi_n)^{-1}$ . This directly follows from the lower bound of the purity, where the

\*timon.schapeler@upb.de

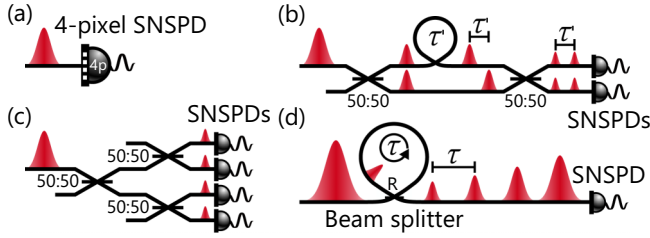


FIG. 1. Schematic representations of (a) a commercially available four-pixel ( $2 \times 2$ ) SNSPD array, (b) a four-bin time-multiplexed detector (eight bins can be achieved with an additional fiber loop of length  $2\tau'$  and beam splitter), (c) a four-bin spatially multiplexed detector, and (d) a ten-bin time-multiplexed loop detector with out-coupling  $R$ , bin separation  $\tau$ , and loop efficiency  $\eta_{\text{loop}}$ , recently shown in [15].

minimal purity coincides with a contribution from every input state in the Hilbert space [17].

The investigated multiplexing schemes [shown in Figs. 1(a)–1(d)] have different dynamic ranges, which means they are sensitive to different numbers of photons. This translates to different Hilbert space dimensions  $M$  in the POVM description. Above a certain photon number, the POVMs of a detector will not change. This can directly be seen in the outcome statistics, as with increasing mean photon numbers, the detector will only respond with the largest outcome. Therefore, the POVM corresponding to that outcome will be saturated (occur with unit probability), while the other POVMs converge to zero probability. This can be seen in Fig. 2, which shows the POVM elements for the four-bin time-multiplexed detector (TMD) as an example.

In order to compare the detector architectures, we use a fixed Hilbert space dimension of  $M = 5000$  without loss of generality, while assuming that the outcome statistics will not change after saturation of the largest outcome. We use Eq. (1) to calculate the purities of the detectors, which are shown in Fig. 3. It can be seen that the detectors with four bins have comparable purities. This is expected, as the choice in the

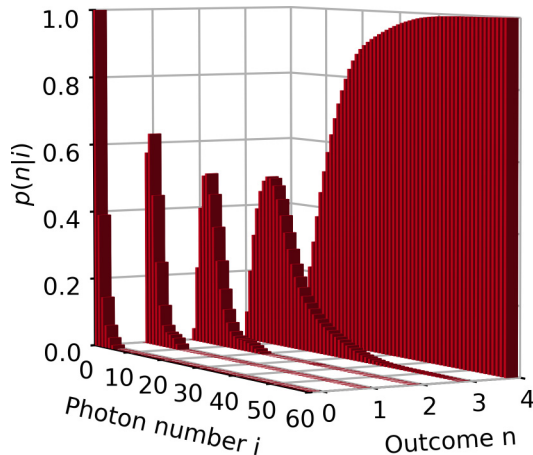


FIG. 2. Diagonal elements of the experimentally reconstructed POVM operators in the photon-number basis for the four-bin time-multiplexed detector, as an example to give a sense of the narrowness of outcomes and show saturation of the largest outcome.

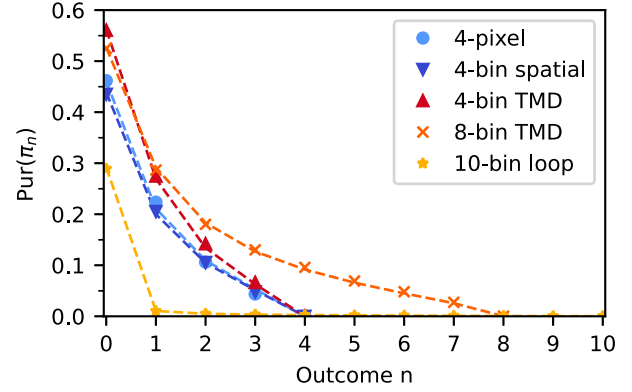


FIG. 3. Purities  $\text{Pur}(\pi_n)$  of the five multiplexed detectors per outcome  $n$ . Different colors and markers correspond to experimental data of the different multiplexing schemes, as labeled in the legend. Dashed lines correspond to modeled data (see the text for details).

degree of freedom of multiplexing (in space or time) should not provide any significant advantages with regard to photon-number resolution. The small differences can be explained by slightly different performance metrics of the detectors (summarized in Table I), with the efficiency being the main contribution, as the purity suffers most for decreasing efficiencies [17]. Figure 3 also shows that the outcome purities of the eight-bin TMD are higher compared to the four-bin TMD. This makes sense, since fewer input states will contribute to each individual outcome, as more outcomes are available in the eight-bin TMD. Narrower POVM distributions imply higher purities.

We verified this behavior by implementing a model of multiplexed click detectors by Miatto *et al.* [18]. We modeled the equal splitting devices (four-pixel, four-bin, and eight-bin TMD and four-bin spatial) by solely their efficiencies (i.e., neglecting noise), which we extracted from the experimental data. The ten-bin loop detector model is based on previous work [19].

The measurement outcome purities closely agree with the experimental data, as can be seen by the dashed lines with corresponding color in Fig. 3. However, having more available outcomes does not directly imply higher outcome purities, as can be seen by the purities of the ten-bin time-multiplexed loop detector in Fig. 3. This is due to the different multiplexing scheme. The device is based on logarithmic multiplexing,

TABLE I. Figures of merit (efficiency  $\eta$ , dark-count probability  $p_{\text{dark}}$ , and crosstalk probability  $p_{\text{xtalk}}$ ) of the five different multiplexed detectors, obtained from the POVMs as in Ref. [21]. The errors are based on assuming 5% uncertainty in the amplitudes of the coherent states.

Detector	$\eta$ (%)	$p_{\text{dark}}$ (%)	$p_{\text{xtalk}}$ (%)
four-pixel	$63 \pm 4$	$(5.9 \pm 1.6) \times 10^{-4}$	$14 \pm 1$
four-bin spatial	$61 \pm 4$	$(5.4 \pm 1.8) \times 10^{-4}$	$3.6 \pm 0.1$
four-bin TMD	$72 \pm 4$	$(1.6 \pm 0.1) \times 10^{-4}$	$< 2 \times 10^{-4}$
eight-bin TMD	$69 \pm 4$	$< 10^{-5}$	$(4.3 \pm 1.1) \times 10^{-5}$
ten-bin loop	$44 \pm 3$	$< 4.1 \times 10^{-5}$	$(4.6 \pm 2.8) \times 10^{-4}$

while the other architectures rely on equal splitting. The ten-bin loop detector responds logarithmically to the number of photons, which results in broad POVM distributions (many orthogonal input states contribute to a given outcome) and thus in poor purities.

### III. INFORMATION EXTRACTION

The purity of a photon-counting detection outcome can be intuitively regarded as the photon-number-resolving ability of the device or the ability of the detector to distinguish between different photon-number states. A related concept is information extraction, namely, how much information about the photon number can be obtained given a specific outcome. Here van Enk [14] introduced the entropy

$$H^{(n)} = - \sum_i p(i|n) \log_2[p(i|n)], \quad (2)$$

which quantifies the information (in bits) about the photon number  $i$  that is still missing after having obtained the outcome  $n$ . This quantity uses the conditional probability  $p(i|n)$ , which describes the probability of having a photon number equal to  $i$  given a measurement outcome  $n$ .

We are able to obtain the probability  $p(i|n)$ , utilizing the POVMs of the detectors. A single element of the POVM  $\pi_n$  is the conditional probability  $p(n|i)$  of  $n$  clicks occurring given  $i$  incident photons. Using Bayes' theorem

$$p(i|n) = \frac{p(n|i)p(i)}{p(n)} = \frac{p(n|i) \sum_{i,n} p(n|i)}{M \sum_i p(n|i)}, \quad (3)$$

it is possible to obtain the probability  $p(i|n)$  directly from the POVMs. Here we assume a flat prior probability  $p(i) = \frac{1}{M}$ , meaning that all input states are equally likely.

From Eq. (2) we can calculate the information that can be extracted by a certain outcome  $n$  about the photon number  $i$  as

$$H_{\text{extr}}^{(n)} = H_{\text{total}}(M) - H^{(n)}, \quad (4)$$

where  $H_{\text{total}}(M) = -\log_2(\frac{1}{M}) = \log_2(M)$  is the total information contained in the Hilbert space of dimension  $M$ . Using Eq. (4), we calculate the amount of information that can be extracted from the Hilbert space of size  $M = 5000$ . The total information available is calculated to  $H_{\text{total}}(5000) = 12.3$  bits, which is shown by the black dashed line in Fig. 4. Having similar performance metrics and outcome purities, the detectors with four bins extract the same amount of information from the Hilbert space. Figure 4 also shows that the outcomes of the eight-bin TMD extract the most information. This directly follows from the argument that more available outcomes lead to narrower POVMs and make each outcome more specific. If a narrow outcome is observed, more knowledge about the photon number can be extracted, as fewer photon-number states (or orthogonal input states) contribute to this outcome. This also explains the sudden drop in the extracted information for the largest outcome of the detectors based on equal splitting. These detectors have a low dynamic range (roughly  $M \approx 100$ ) compared to the maximum Hilbert space of size  $M = 5000$ . This means that obtaining the largest outcome reveals very little about the possible input photon number, due to the saturation of the outcome (compare Fig. 2).

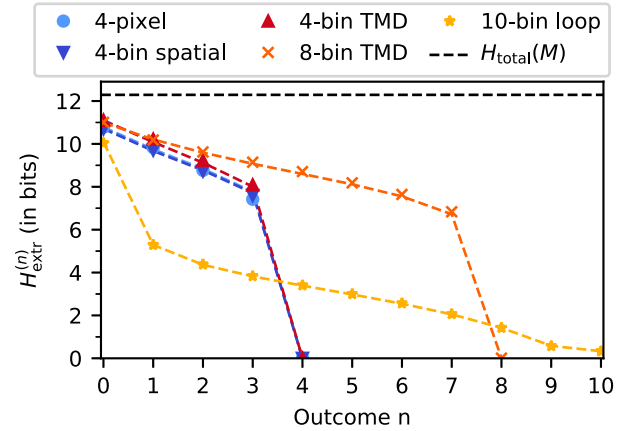


FIG. 4. Extracted information  $H_{\text{extr}}^{(n)}$  in bits of the five multiplexed detectors per outcome  $n$ . The total available information in the Hilbert space of dimension  $M = 5000$  is shown by the black dashed line. Different colors and markers correspond to experimental data of the different multiplexing schemes, as labeled in the legend. Dashed lines correspond to modeled data (see the text for details).

The outcomes of the ten-bin loop detector, based on logarithmic multiplexing, span the Hilbert space with broad POVM distributions. This leads to less information extracted per outcome. However, even the largest outcome is able to extract some information from the total available Hilbert space, even for large input states with hundreds to thousands of photons. From this, it is clear that solely increasing the number of multiplexing outcomes will not yield better photon-number resolution. Optimizing the photon-number-resolving ability of a device requires optimizing the splitting between multiplexed detectors [17].

### IV. EXPERIMENTAL METHODS

Calculating the purity and information extraction relies on a tomographic reconstruction of each detector. We summarize the methods here; more detail can be found in Refs. [16,19–21].

In order to reconstruct the POVMs, the detector under test needs to be subjected to a set of input states

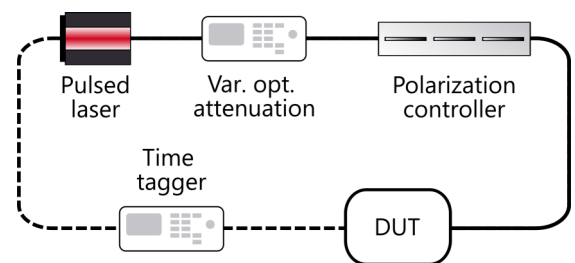


FIG. 5. Experimental setup for the detector tomography analysis. A 1556-nm pulsed laser produces coherent states, which can be attenuated by variable optical attenuators. The polarization can be controlled to optimize detection efficiencies for the polarization-dependent SNSPDs, which are connected next. A time tagger records the electrical responses from the detectors. Solid and dashed lines represent optical and electrical connections, respectively.

TABLE II. Total counts in thousands with corresponding uncertainties for the four-pixel detector.

$ \alpha ^2$	$n = 1$	$n = 2$	$n = 3$	$n = 4$
333(22)	4990.2(23)	4992.5(23)	4993.2(23)	4994.2(23)
290(19)	4997.7(23)	4991.2(23)	4993.1(23)	4992.2(23)
253(17)	4991.0(23)	4993.6(23)	4992.5(23)	4993.7(23)
221(15)	4991.2(23)	4992.8(23)	4991.6(23)	4993.1(23)
193(13)	4990.6(23)	4991.3(23)	4993.9(23)	4993.9(23)
168(11)	4999.7(23)	4992.1(23)	4992.6(23)	4991.7(23)
147(10)	4990.8(23)	4992.1(23)	4992.9(23)	4991.6(23)
123(8)	4989.7(23)	4994.0(23)	4991.6(23)	4992.9(23)
102(7)	4990.6(23)	4993.4(23)	4992.2(23)	4991.9(23)
82(6)	4990.8(23)	4993.2(23)	4992.3(23)	4991.4(23)
65(5)	4990.8(23)	4993.7(23)	4992.5(23)	4984.1(23)
50(4)	4990.5(23)	4993.3(23)	4993.3(23)	4954.9(23)
36.0(24)	4999.0(23)	4993.0(23)	4993.0(23)	4844.9(23)
25.1(17)	4988.0(23)	4992.5(23)	4981.1(23)	4508.6(22)
15.9(11)	4991.8(23)	4984.4(23)	4840.5(23)	3587.7(19)
9.2(6)	4979.7(23)	4832.5(22)	4037.9(21)	2014.8(15)
4.09(27)	4617.3(22)	3490.0(19)	1747.4(14)	445.4(7)
1.00(7)	2340.0(16)	845.2(10)	148.8(4)	17.46(14)
0	1.90(5)	0.150(13)	0(1)	0(1)

spanning the Hilbert space of the given device. Coherent states are an ideal choice, as they form a tomographically complete set [16]. Here we compare four different multiplexing schemes (five detectors) in total: a commercially available four-pixel SNSPD array, a four-bin (and eight-bin) TMD, a four-bin spatially multiplexed detector, and finally a ten-bin time-multiplexed loop detector, which relies on a logarithmic time-multiplexing architecture enabling a high dynamic range over 120 dB [15] [all shown in Figs. 1(a)–1(d)]. The experimental setup, shown schematically in Fig. 5, begins with a pulsed laser producing coherent states with a wavelength of 1556 nm. The mean photon number can be controlled by variable optical attenuators and the polarization can be set to optimize the detection efficiency of the polarization-dependent SNSPDs. Afterward, the different multiplexing

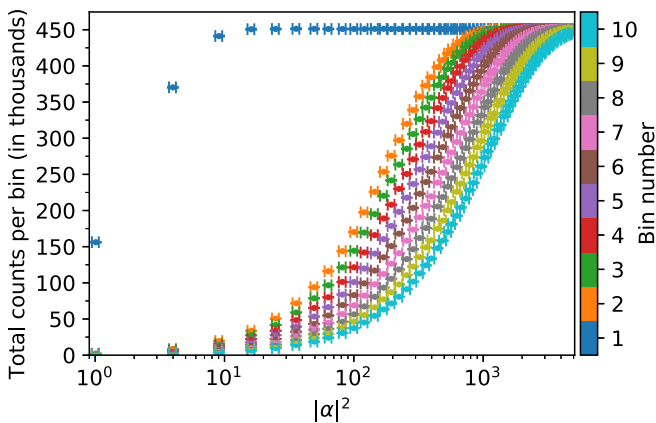


FIG. 6. Total counts per bin for the ten-bin time-multiplexed loop detector vs mean photon number of the coherent probe states with corresponding uncertainties. The uncertainty in the total counts is too small to resolve.

TABLE III. Total counts in thousands with corresponding uncertainties for the four-bin spatially multiplexed detector. Here  $D_1$ – $D_4$  correspond to the four detectors.

$ \alpha ^2$	$D_1$	$D_2$	$D_3$	$D_4$
122(8)	4997.5(23)	4997.5(23)	4997.5(23)	4997.1(23)
102(7)	4997.8(23)	4997.8(23)	4997.8(23)	4997.4(23)
81(6)	4998.2(23)	4998.4(23)	4998.4(23)	4998.1(23)
65(5)	4996.6(23)	4998.1(23)	4998.4(23)	4997.9(23)
49(4)	4986.1(23)	4994.3(23)	4998.1(23)	4995.8(23)
35.9(23)	4931.0(23)	4968.7(23)	4993.8(23)	4978.8(23)
25.0(17)	4760.6(22)	4863.6(23)	4957.2(23)	4898.7(23)
16.6(11)	4345.7(21)	4551.4(22)	4793.5(22)	4631.0(22)
9.2(6)	3365.1(19)	3676.5(20)	4143.8(21)	3813.0(20)
4.08(27)	1923.0(14)	2194.5(15)	2676.4(17)	2326.7(16)
1.05(7)	590.3(8)	695.4(9)	900.7(10)	751.5(9)
0	0.101(11)	0.134(12)	0.348(19)	1.44(4)

schemes are connected and the outcome statistics are recorded by a time tagger in a few-nanosecond-wide coincidence window. The mean photon numbers of the coherent input states are chosen to scale quadratically to efficiently span the Hilbert space of the different detectors. Different numbers of input states are necessary, as the Hilbert space dimension depends on the detector under test.

The raw data (see the Appendix for total counts for all different detectors) are converted to the outcome statistic matrix  $\mathbf{P}$ , depending on the form of the acquired counts. This conversion is described in detail in Ref. [21] for the four-pixel detector, in Ref. [22] for the four-bin spatially multiplexed detector, and in Ref. [19] for the ten-bin loop detector. For the four- and eight-bin TMDs, the total counts (given in Tables IV and V, respectively) are divided by the total number of input pulses to obtain  $\mathbf{P}$ . After knowing the input states, typically represented by a matrix  $\mathbf{F}$ , it is possible to reconstruct the POVM matrix  $\mathbf{\Pi}$  of the different multiplexed detectors. This is done using the Born rule, which allows one to formulate the matrix equation  $\mathbf{P} = \mathbf{F}\mathbf{\Pi}$  and a subsequent matrix inversion routine [23–25].

TABLE IV. Total counts in thousands with corresponding uncertainties for the four-bin TMD.

$ \alpha ^2$	$n = 0$	$n = 1$	$n = 2$	$n = 3$	$n = 4$
49(4)	0(1)	0(1)	0(1)	0.046(7)	100.0(4)
40.1(26)	0(1)	0(1)	0(1)	0.210(15)	99.8(4)
31.3(21)	0(1)	0(1)	0.007(2)	1.17(4)	98.8(4)
23.9(16)	0(1)	0(1)	0.071(9)	4.44(7)	95.5(4)
17.9(12)	0(1)	0.019(5)	0.686(27)	13.01(12)	86.3(3)
12.2(8)	0.010(4)	0.359(19)	5.13(8)	30.32(18)	64.18(26)
8.0(6)	0.269(17)	3.62(7)	19.01(14)	42.25(21)	34.85(19)
4.45(29)	4.08(7)	20.17(15)	36.92(20)	29.98(18)	8.85(10)
1.99(13)	24.10(16)	41.00(21)	26.44(17)	7.58(9)	0.839(29)
0.49(4)	70.20(27)	25.90(17)	3.72(7)	0.190(14)	0.005(2)
0.050(4)	96.4(4)	3.51(6)	0.055(8)	0(1)	0(1)
0.0051(4)	99.6(4)	0.377(20)	0.002(1)	0(1)	0(1)
0.00052(4)	100.0(4)	0.042(7)	0(1)	0(1)	0(1)
0	100.0(4)	0(1)	0(1)	0(1)	0(1)



TABLE V. Total counts in thousands with corresponding uncertainties for the eight-bin TMD.

$ \alpha ^2$	$n = 0$	$n = 1$	$n = 2$	$n = 3$	$n = 4$	$n = 5$	$n = 6$	$n = 7$	$n = 8$
98(7)	0(1)	0(1)	0(1)	0(1)	0(1)	0(1)	0(1)	0.102(11)	99.9(4)
80(6)	0(1)	0(1)	0(1)	0(1)	0(1)	0(1)	0(1)	0.558(24)	99.4(4)
63(5)	0(1)	0(1)	0(1)	0(1)	0(1)	0.001(1)	0.033(6)	2.82(6)	97.1(4)
48(4)	0(1)	0(1)	0(1)	0(1)	0(1)	0.012(4)	0.459(22)	9.8(1)	89.7(3)
35.7(23)	0(1)	0(1)	0(1)	1(1)	0.013(4)	0.305(18)	3.66(7)	24.84(16)	71.18(27)
24.4(16)	0(1)	0.001(1)	0.005(2)	0.067(9)	0.686(27)	4.57(7)	17.81(14)	39.2(2)	37.7(2)
15.9(11)	0.002(1)	0.035(6)	0.304(18)	2.09(5)	8.2(1)	20.36(15)	31.23(18)	27.42(17)	10.320(11)
8.9(6)	0.198(15)	2.00(5)	8.3(1)	19.00(14)	26.89(17)	24.63(16)	13.83(12)	4.53(7)	0.610(25)
3.97(26)	6.39(8)	21.44(15)	30.26(18)	24.51(16)	12.41(12)	4.08(7)	0.807(29)	0.10(1)	0.003(1)
0.99(7)	50.80(23)	35.84(19)	11.18(11)	1.93(5)	0.230(16)	0.015(4)	0(1)	0(1)	0(1)
0.100(7)	93.3(4)	6.48(9)	0.202(15)	0.002(1)	0(1)	0(1)	0(1)	0(1)	0(1)
0.0102(7)	99.3(4)	0.692(27)	0.006(2)	0(1)	0(1)	0(1)	0(1)	0(1)	0(1)
0.00104(5)	99.9(4)	0.073(9)	0(1)	0(1)	0(1)	0(1)	0(1)	0(1)	0(1)
0	100.0(4)	0(1)	0(1)	0(1)	0(1)	0(1)	0(1)	0(1)	0(1)

## V. CONCLUSION

We have shown that quantum detector tomography is the basis to enable a comparison of different multiplexing schemes. The outcome purity, which can be calculated directly from the POVM elements of given detection outcomes, indicates how pure a certain outcome is. Quantum detector tomography enables a mapping to photon-number states; thus the purity gives insight into the photon-number-resolving ability of the devices. Narrow POVM distributions are purer, in the sense that fewer photon-number states contribute to the given outcome. This directly translates into the amount of information the outcome can extract from the total available Hilbert space. More information can be extracted by narrow POVM distributions. Outcomes of multiplexing architectures based on equal splitting, such as standard spatial or temporal multiplexing, show significantly better purities and can extract larger amounts of information compared to the logarithmic multiplexing scheme of the ten-bin loop detector. Nevertheless, logarithmic multiplexing enables a high dynamic range, which gives information about large photon numbers, where the equal splitting schemes are already saturated. Our analysis further confirms that more multiplexing outcomes enable higher photon-number-resolving ability [6,26,27], but also that the splitting between those outcomes must be optimized.

## ACKNOWLEDGMENT

This work was supported by the Bundesministerium für Bildung und Forschung (Grant No. 13N14911).

## APPENDIX: MEASUREMENT DATA

The total counts of the five different multiplexing architectures are shown in Tables II–V and Fig. 6. The uncertainty of the mean photon number of the coherent input states is based on assuming 5% uncertainty for the calibration detector efficiency. The uncertainty of the total counts is calculated using Poisson statistics, i.e., the square root of the total counts. The uncertainty of the total counts is negligible in comparison to the uncertainty in the coherent state mean photon number.

For the four-pixel detector and the four-bin spatially multiplexed detector, data were recorded for 10 s at a repetition rate of 500 kHz, leading to a maximum of  $5 \times 10^6$  total counts in Tables II and III. For the four-bin and eight-bin TMDs, data were recorded for 1 s at a repetition rate of 100 kHz, leading to a maximum of  $1 \times 10^5$  total counts in Tables IV and V. For the ten-bin time-multiplexed loop detector, data was recorded for 30 s at a repetition rate of 15 kHz, leading to a maximum of  $4.5 \times 10^5$  total counts in Fig. 6.

- [1] C. You, M. Hong, P. Bierhorst, A. E. Lita, S. Glancy, S. Kolthammer, E. Knill, S. W. Nam, R. P. Mirin, O. S. Magaña-Loaiza, and T. Gerrits, Scalable multiphoton quantum metrology with neither pre- nor post-selected measurements, *Appl. Phys. Rev.* **8**, 041406 (2021).
- [2] R. H. Hadfield, Single-photon detectors for optical quantum information applications, *Nat. Photon.* **3**, 696 (2009).
- [3] P.-A. Moreau, E. Toninelli, T. Gregory, and M. J. Padgett, Imaging with quantum states of light, *Nat. Rev. Phys.* **1**, 367 (2019).
- [4] A. Migdall, S. V. Polyakov, J. Fan, and J. C. Bienfang, *Single-Photon Generation and Detection: Physics and Applications* (Academic Press, New York, 2013).
- [5] B. Cabrera, R. M. Clarke, P. Colling, A. J. Miller, S. Nam, and R. W. Romani, Detection of single infrared, optical, and ultra-violet photons using superconducting transition edge sensors, *Appl. Phys. Lett.* **73**, 735 (1998).
- [6] R. Kruse, J. Tiedau, T. J. Bartley, S. Barkhofen, and C. Silberhorn, Limits of the time-multiplexed photon-counting method, *Phys. Rev. A* **95**, 023815 (2017).
- [7] H. Paul, P. Törmä, T. Kiss, and I. Jex, Photon Chopping: New Way to Measure the Quantum State of Light, *Phys. Rev. Lett.* **76**, 2464 (1996).
- [8] D. Achilles, C. Silberhorn, C. Śliwa, K. Banaszek, and I. A. Walmsley, Fiber-assisted detection with photon number resolution, *Opt. Lett.* **28**, 2387 (2003).
- [9] M. J. Fitch, B. C. Jacobs, T. B. Pittman, and J. D. Franson, Photon-number resolution using time-multiplexed single-photon detectors, *Phys. Rev. A* **68**, 043814 (2003).

- [10] E. A. Dauler, B. S. Robinson, A. J. Kerman, J. K. W. Yang, K. M. Rosfjord, V. Anant, B. Voronov, G. Gol'tsman, and K. K. Berggren, Multi-element superconducting nanowire single-photon detector, *IEEE Trans. Appl. Supercond.* **17**, 279 (2007).
- [11] K. Banaszek and I. A. Walmsley, Photon counting with a loop detector, *Opt. Lett.* **28**, 52 (2003).
- [12] Q. Yu, K. Sun, Q. Li, and A. Beling, Segmented waveguide photodetector with 90% quantum efficiency, *Opt. Express* **26**, 12499 (2018).
- [13] M. Bohmann, R. Kruse, J. Sperling, C. Silberhorn, and W. Vogel, Direct calibration of click-counting detectors, *Phys. Rev. A* **95**, 033806 (2017).
- [14] S. J. van Enk, Photodetector figures of merit in terms of POVMs, *J. Phys. Commun.* **1**, 045001 (2017).
- [15] J. Tiedau, E. Meyer-Scott, T. Nitsche, S. Barkhofen, T. J. Bartley, and C. Silberhorn, A high dynamic range optical detector for measuring single photons and bright light, *Opt. Express* **27**, 1 (2019).
- [16] J. S. Lundeen, A. Feito, H. Coldenstrodt-Ronge, K. L. Pregnell, C. Silberhorn, T. C. Ralph, J. Eisert, M. B. Plenio, and I. A. Walmsley, Tomography of quantum detectors, *Nat. Phys.* **5**, 27 (2009).
- [17] R. Nehra, C.-H. Chang, Q. Yu, A. Beling, and O. Pfister, Photon-number-resolving segmented detectors based on single-photon avalanche-photodiodes, *Opt. Express* **28**, 3660 (2020).
- [18] F. M. Miatto, A. Safari, and R. W. Boyd, Explicit formulas for photon number discrimination with on/off detectors, *Appl. Opt.* **57**, 6750 (2018).
- [19] T. Schapeler, J. P. Höpker, and T. J. Bartley, Quantum detector tomography of a high dynamic-range superconducting nanowire single-photon detector, *Supercond. Sci. Technol.* **34**, 064002 (2021).
- [20] A. Feito, J. S. Lundeen, H. Coldenstrodt-Ronge, J. Eisert, M. B. Plenio, and I. A. Walmsley, Measuring measurement: theory and practice, *New J. Phys.* **11**, 093038 (2009).
- [21] T. Schapeler, J. P. Höpker, and T. J. Bartley, Quantum detector tomography of a  $2 \times 2$  multi-pixel array of superconducting nanowire single photon detectors, *Opt. Express* **28**, 33035 (2020).
- [22] T. Schapeler, Quantum detector tomography of superconducting detector arrays, M.Sc. thesis, Paderborn University, 2020, doi:10.17619/UNIPB/1-1374.
- [23] T. Schapeler, Detector tomography python code, available at <https://physik.uni-paderborn.de/fileadmin/physik/Arbeitsgruppen/bartley/Downloads/Detector-Tomography-CVXPY-Python-Timon-Schapeler.zip> (2020).
- [24] S. Diamond and S. Boyd, CVXPY: A Python-embedded modeling language for convex optimization, *J. Mach. Learn. Res.* **17**, 1 (2016).
- [25] A. Agrawal, R. Verschueren, S. Diamond, and S. Boyd, A rewriting system for convex optimization problems, *J. Control Decis.* **5**, 42 (2018).
- [26] J. Sperling, W. Vogel, and G. S. Agarwal, True photocounting statistics of multiple on-off detectors, *Phys. Rev. A* **85**, 023820 (2012).
- [27] M. Jönsson and G. Björk, Evaluating the performance of photon-number-resolving detectors, *Phys. Rev. A* **99**, 043822 (2019).